IOPscience iopscience.iop.org

Home Search Collections Journals About Contact us My IOPscience

Molecular dynamics simulation based evaluation of glass transition temperatures of polystyrene in the presence of carbon dioxide

This content has been downloaded from IOPscience. Please scroll down to see the full text.

2010 Modelling Simul. Mater. Sci. Eng. 18 065003

(http://iopscience.iop.org/0965-0393/18/6/065003)

View the table of contents for this issue, or go to the journal homepage for more

Download details:

IP Address: 128.220.159.1
This content was downloaded on 03/08/2016 at 19:13

Please note that terms and conditions apply.

Modelling Simul. Mater. Sci. Eng. **18** (2010) 065003 (22pp) doi:10.1088/0965-0393/18/6/065003

Molecular dynamics simulation based evaluation of glass transition temperatures of polystyrene in the presence of carbon dioxide

Anand Srivastava[1], **Coleman Alleman**[1], **Somnath Ghosh**[1,3] **and L J Lee**[2]

[1] Computational Mechanics Research Laboratory, Department of Mechanical Engineering, The Ohio State University, Columbus, OH 43210, USA
[2] Department of Chemical and Biomolecular Engineering, The Ohio State University, Columbus, OH 43210, USA

E-mail: ghosh.5@osu.edu

Received 3 December 2009, in final form 7 June 2010
Published 2 July 2010
Online at stacks.iop.org/MSMSE/18/065003

Abstract

This paper develops a detailed molecular dynamics (MD) simulation model to study the glass transition temperature (T_g) of a finite polystyrene (PS) system in the presence of high pressure carbon dioxide (CO_2). Validated inter-atomic potentials for pure PS and CO_2 are used for these simulations. Specific parameters and combinations rules are introduced to accurately model the intermolecular interactions between PS and CO_2. The intermolecular interaction model has a strong effect on the T_g of the PS–CO_2 system. The MD model comprises PS and CO_2 molecules confined in a finite walled system to manifest the effects of high pressure CO_2. The effectiveness of the simulation model is established by comparison with experimental free-volume data from positronium annihilation lifetime spectroscopy (PALS). An important outcome of this study is the identification of clearly demarcated regions for bulk and surface analysis. Physical properties such as density, free volume, segmental motion across the thickness and end group mobility are also studied to gain insight into the polymer dynamics. As is expected, the simulations show that the presence of high pressure CO_2 reduces the T_g of PS significantly due to an increase in chain mobility. Additionally, the simulation data show a remarkable effect of CO_2 on the extent and characteristics of the surface layer.

(Some figures in this article are in colour only in the electronic version)

[3] Author to whom any correspondence should be addressed.

 © 2010 IOP Publishing Ltd Printed in the UK & the USA

1. Introduction

The development of special techniques for bonding nanoscale polymer devices is currently a priority in the medical industry for various drug delivery applications. While mechanically stable polymer nanostructures of sizes less than 20 nm can be fabricated by techniques such as nanoimprint lithography [1], focused ion beam methods [2] and dip pen nanolithography (DPN) [3], bonding of such structures at scales lower than 100 nm is currently not achievable. This is because conventional bonding techniques rely on high temperatures or chemical adhesives. Elevated temperatures induce residual stresses that cause warping in the nanoscale structures and denature the biomolecules that must be present in the fabrication of some devices. Chemical adhesives are impractical due to their tendency to obstruct nanoscale features such as nanochannels and nanopores. Thus, processes that are biologically benign and also preserve nanoscale features must be developed to allow the fabrication of bonded polymer biomedical nanodevices at environments near room temperature. Carbon dioxide (CO_2) assisted polymer processing is one such method which is widely gaining acceptance for fabrication of polymer nanostructures [4–6].

Carbon dioxide is a widely used processing solvent in the polymer industry [7, 8]. The strength of CO_2 as a processing solvent lies in its high diffusivity and liquid like solubility [9]. Properties like glass transition temperature (T_g) are shown to decrease in a CO_2 environment [10, 11]. Positronium lifetime annihilation spectroscopy (PALS) experiments, developed in [11] and summarized in section 2, have shown that in a CO_2 environment the amount of free volume in polystyrene (PS) increases significantly. This can depress the glass transition temperature (T_g) by more than 50 K. Thermodynamics based models [12–16] also predict reductions in T_g for polymers with increasing pressure of CO_2. This reduction in T_g facilitates processing of polymer at near room-temperature conditions. Even at relatively high pressures, CO_2 has very little impact on bioactivity when compared with the effects at elevated temperature [6]. Moreover, the depression in T_g is more pronounced at the polymer surface, allowing the inter-diffusion of surface molecules during bonding while leaving intact geometric features with sizes much larger than the surface-affected depths [4, 6, 11]. *In situ* Bragg diffraction and *ex situ* SEM microscopy based tests have shown [4] that the dissolved CO_2 provides the mobility for the polymer chains at the interface needed for welding. Low temperature fusion of polymeric structure using CO_2 has been successfully carried out for sub-micrometer structures in [5, 6]. However, the CO_2 enabled processes have been unable to reliably produce satisfactory bonding in devices with dimensions less than 100 nm. Optimization of CO_2 assisted polymer processing techniques is therefore a considerable design challenge for the fabrication of biomedical nanodevices by polymer bonding. Robust understanding of the effect of CO_2 on polymer chain dynamics is essential for fabrication of optimally small devices.

A considerable amount of theoretical and simulation work has been carried out with the goal of understanding the effects of CO_2 on PS [12–16]. However, most of these models are for bulk PS–CO_2 binary systems and the results can be applied to large PS system processing only. Fabricating nanostructures using CO_2 assisted polymer processing technology requires additional knowledge about the interface. For example, the extent of the surface layer as a function of CO_2 pressure is used as one of the polymer-bonding design parameters for nanoscale fabrication. Molecular-level simulations are needed to provide insights into the underlying mechanisms for developing robust design tools that can optimize CO_2 assisted polymer processing. Molecular dynamics (MD) and Monte Carlo simulations have been carried out on bulk and finite thin film polymeric materials in [17–19]. Most of these models are phenomenological in nature and the simulation is carried out on simple models such as the bead-spring model [18, 20] and the hard-sphere MD model [19]. Moreover, simulations at

high pressure are mostly done for bulk periodic systems [21]. The literature is sparse for high pressure finite systems [22] because of the complications in applying external pressure to a finite MD system [23]. As shown in [22], the finite system is generally embedded in a fluid that serves as a pressure reservoir and the fluid is prevented from diffusing into the finite system by intermolecular repulsion. However, an additional challenge in this work comes from the fact that the pressure-inducing agent CO_2 is also a solvent. Consequently, a novel simulation model is developed in this work, which consists of a finite PS–CO_2 system. The CO_2 acts both as a plasticizing and pressure-inducing agent. This MD model is able to accurately predict changes in T_g and density variations, as well as provide information on surface characteristics such as density profiles.

MD simulations of binary gas-polymer systems have been performed with the objectives of studying gas diffusion and solubility in polymers [24–27]. However, literature on MD modeling of PS–CO_2 systems is sparse with respect to calculation of glass transition temperatures. One MD model for PS–CO_2 systems in [27] predicts T_g for bulk PS and the sorption of CO_2 in PS. This model does not accurately predict the swelling of PS in the presence of absorbed CO_2 due to its limitations in PS–CO_2 interaction parameters, ensemble representation and applied boundary conditions. These limitations are overcome in this study through an explicit molecular scale computational model of a nanoscale PS–CO_2 binary system with finite (as opposed to periodic) boundaries. Results of the MD simulations in this study are validated with PALS-based experimental observations in [11, 28]. The simulation results provide an enhanced understanding of the effect of CO_2 on the surface-affected region of the finite PS system. Section 2 provides a brief description of the PALS experiment that provides the framework for the design of the current MD model. The development of the MD simulation model is explained in section 3. This section includes initial system setup, design of potential functions for the materials involved and the pre-simulation equilibration to prepare the sample for production runs. The results are reported and discussed in section 4, with concluding remarks in section 5.

2. Experimental methods for determining glass transition temperature

Though conventional methods such as dilatometry and differential scanning calorimetry (DSC) provide good results for bulk polymer systems, the positronium annihilation lifetime spectroscopy (PALS) [28–30] is now established as one of the most effective experimental methods for measuring the nanoscale size of voids in polymeric materials. The success of PALS is attributed to the small size of the positronium probe ($\sim$1.6 Å), which makes it particularly sensitive to nanoscale holes and cavities. Not only does it measure cavity size and the free-volume fraction (f_v), it also provides information on the distribution of free volume in the material in the 1–10 Å range. PALS experiments on PS–CO_2 system have been carried out recently in [11] and these results form the basis for validation of the present molecular model.

A schematic of the experimental setup can be found in [31, 32]. Their studies have shown that T_g decreases with increasing pressures of CO_2, with approximately 50 K difference in T_g between ambient and 400 psi CO_2 conditions. Results of the PALS experiments are shown in figure 1. The drop in T_g can be attributed to the solubilization of CO_2, which acts as a plasticizing agent, creating a substantial amount of free volume. Experiments are not able to clearly discern the underlying molecular-level physics involved in this T_g depression. The MD model in this study provides the framework needed to explain the experimental observations by facilitating study of the atomic-scale interactions that govern the T_g effects.

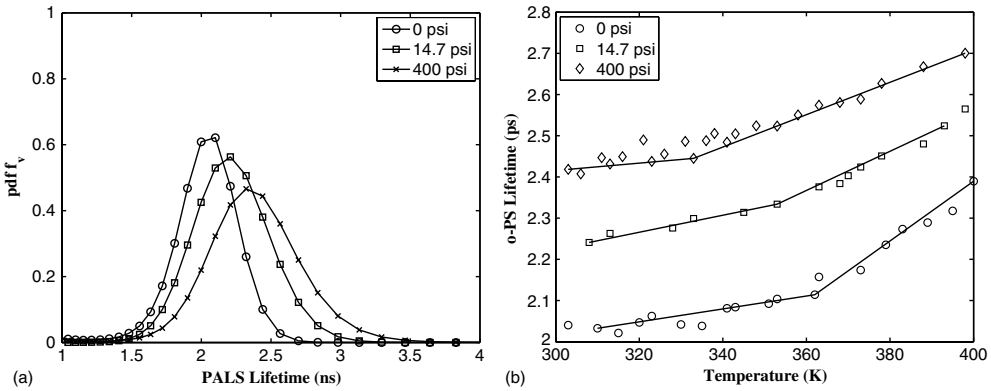

Figure 1. (*a*) Ortho-Ps lifetime distribution (free-volume radius) of PS at ambient temperature and different pressures of CO_2. (*b*) The glass transition temperature determined by PALS for different pressures of CO_2 [11].

3. MD model of the PS–CO_2 system

The MD model is developed to accurately reproduce the experimental conditions of PS immersed in a CO_2 environment. Periodic boundary conditions, simulated with an applied virial pressure, do not yield experimental values for specific volume and T_g. This limitation is overcome by introducing a finite volume system for MD simulations. PS droplet and CO_2 molecules are confined to a fixed domain of finite size and the simulation is run with an NVT ensemble. The walls of this finite system are constructed by a uniform grid of frozen wall atoms. Rapidly decaying repulsive interaction potentials between the boundary atoms and the PS and CO_2 atoms, of the form $U_w(r) = A \times r^{-12}$ are implemented to confine the molecules within the system. Details of the molecular PS–CO_2 system are provided below.

3.1. Molecular representation of system constituents

Validated inter-atomic potentials for PS [33, 34] and CO_2 [35] are used in the model. Additionally, this study requires the development of the cross-constituent interaction parameters between PS and CO_2.

3.1.1. Representation of PS. Figure 2(*a*) shows an explicit representation of a PS monomer. A united atom model of the structure that invokes coarse graining to reduce the degrees of freedom is shown in figure 2(*b*). In the united atom representation, each PS monomer is represented by eight united atoms, C_1 to C_8, of five different types. The two outer backbone units for each PS chain, CH_3, and the inner backbone unit, CH_2, are represented by C_1. The other inner backbone unit CH is represented by C_2 in the united atom model. The C_3 unit corresponds to the aromatic carbon atom without the hydrogen (C_{AR}) and the units C_4 to C_8 represent the aromatic carbon atom with hydrogen (C_{AH}) in the phenyl ring.

The effect of coarse graining an alkane chain with a united atom representation is studied in [36, 37] and it is shown that the frequency of –C–H– bond vibrations have no effect on properties like T_g and modulus. Hence, hydrogen can be safely coarse-grained with carbon atom for this study. Since the highest frequency –C–H– vibrations are suppressed due to united atom representation, the time step of simulation can be safely increased by four times. Moreover, twice the number of molecules can be simulated with the same computational

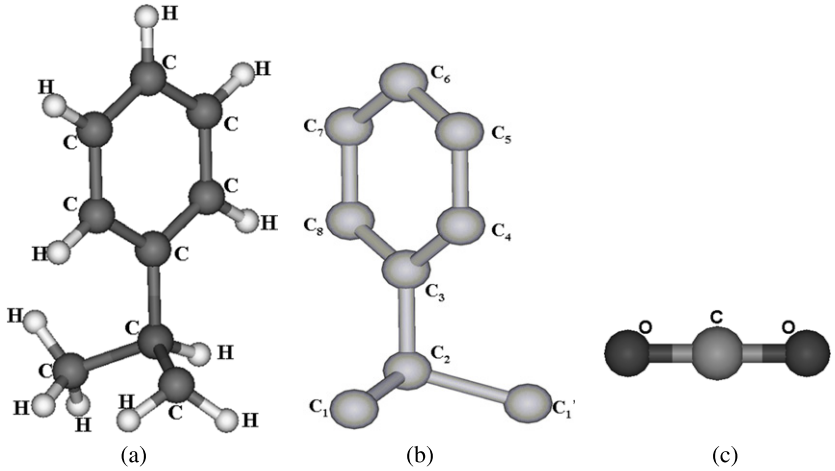

Figure 2. (*a*) PS monomer, (*b*) United atom representation and (*c*) CO_2 molecule.

resources available, as hydrogen is no longer explicitly represented. However, representing –C–H– as one united atom neutralizes the dipolar charges in the electronic structure of the phenyl ring. This can marginalize the model if charged interactions are involved and needs to be taken care of if required. The final system in this study involves PS interaction with a highly polarized CO_2 molecule. As a result, the PS–CO_2 interactions are carefully chosen to countermand the drawbacks due to loss of charges on PS molecule which would have affected the final results. The details are in section 3.1.3, where PS–CO_2 interaction potential parameters are discussed in detail.

The molecular force field for PS consists of intra-molecular or bonded and intermolecular or non-bonded interactions. Correspondingly, the total potential energy is additively decomposed as

$$U_{\text{total}} = U_{\text{non-bonded}} + U_{\text{bonded}}. \tag{1}$$

Important parameters for the bonded and non-bonded interactions are obtained from the TraPPE force field in [33, 34], and are reported in table 1. The van der Waals interactions between atoms of type i and j are represented through the Lennard-Jones (LJ) potential function,

$$U_{nb}^{\text{LJ}}(r_{ij}) = \sum 4\varepsilon_{ij}\left[\left(\frac{\sigma_{ij}}{r_{ij}}\right)^{12} - \left(\frac{\sigma_{ij}}{r_{ij}}\right)^{6}\right], \tag{2}$$

where ε_{ij} is the well depth of the potential and σ_{ij} is the distance at which the potential goes to zero. The non-bonded potential in equation (2) is applied to united atom pairs from different chains and those belonging to the same chain but not governed by bonded-type interactions. The bonded potential effectively accounts for the kinematics and conformational forms of PS including angle-bending, torsional motions around the dihedral angles, and out of plane forces as suggested in [33, 34], i.e.

$$U_{\text{bonded}} = U_{\text{stretch}} + U_{\text{angle}} + U_{\text{torsion}} + U_{\text{others}}. \tag{3}$$

All the bond lengths in table 1 are kept constant. The bond stretch degree of freedom is suppressed, as the time scale of bond vibration has no effect on T_g. The SHAKE algorithm described in [38] is used with a relative tolerance of 10^{-6} to apply the bond constraint for the

Table 1. Potential function parameters for united atom representation of PS system.

LJ parameters	ε (kJ mol^{-1})	σ (Å)	
$C_1(CH_3)$	0.8159	3.750	
$C_1(CH_2)$	0.3828	3.950	
$C_2(CH)$	0.0831	4.650	
$C_3(C_{AR})$	0.2494	3.700	
C_4 to C_8 (C_{AH})	0.4197	3.695	
	Chemical bonds	r_0(Å)	
	CH_3–CH	1.54	
	CH_2–CH	1.54	
	CH–C_{AR}	1.51	
	C_{AH}–C_{AR}	1.40	
	C_{AH}–C_{AH}	1.40	
Angular bonds	k_θ (kJ mol^{-1} rad^{-2})	θ_0 (°)	
CH_3/CH_2–CH–CH_2/CH_3	520.0	112.0	
CH–CH_2–CH	520.0	114.0	
C_{AR}–C_{AH}–C_{AH}	1000.0	120.0	
C_{AH}–C_{AH}–C_{AH}	1000.0	120.0	
CH–C_{AR}–C_{AH}	1000.0	120.0	
Dihedral bonds	A_1 (kJ mol^{-1})	A_2 (kJ mol^{-1})	A_3 (kJ mol^{-1})
CH_3/CH_2–CH–CH_2–CH	5.904	−1.124	13.158
Improper bonds	k_ψ (kJ mol^{-1} rad^{-2})	ψ_0 (°)	
C_{AR}–C_{AH}–C_{AH}–C_{AH}	167.40	0.00	
C_{AR}–C_{AH}–C_{AH}–C_{AH}	167.40	0.00	
CH_2–CH–C_{AR}–C_{AH}	167.40	0.00	
CH–CH_3/CH_2–CH_2–C_{AR}	334.80	35.26	

rigid bonds. For the bonded interactions, the functional form for bond angle bending modes are described using an harmonic potential,

$$U_{\text{angle}} = \frac{K_\theta}{2}(\theta_k - \theta_0)^2, \tag{4}$$

where values for the constants K_l, l_0, K_θ and θ_0 are listed in table 1. The functional form for the torsional interaction describes the rotation along bonds in the backbone carbon atoms. According to the transferable potentials for phase equilibria (TraPPE), it is chosen to have the form

$$U_{\text{torsion}} = \tfrac{1}{2}\{A_1(1 + \cos(\phi)) + A_2(1 - \cos(2\phi)) + A_3(1 + \cos(3\phi))\}. \tag{5}$$

The parameters are listed in table 1. The dihedral potential does not account for the distance dependent 1–4 interactions. One of the artifacts of coarse graining is the possibility of loss in configurational integrity due to removal of hydrogen atoms at chiral centers. As a result, the four united atoms, C_1, C_2, C_3 and C_1' tend to collapse into one plane. In order to prevent this

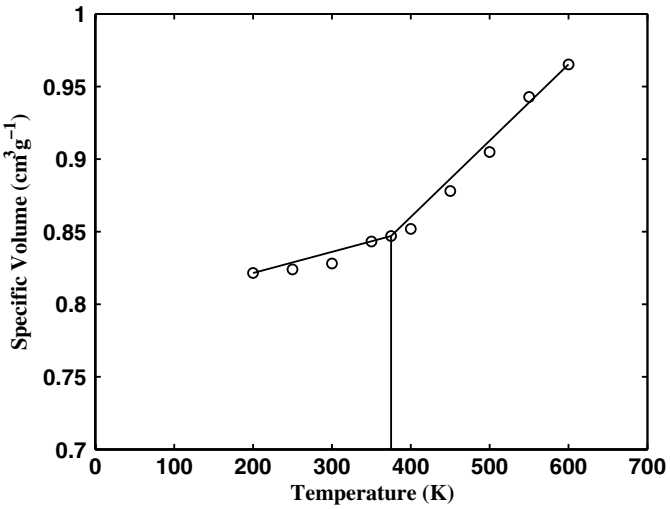

Figure 3. Specific volume–temperature plot with the location of change in slope representing T_g at ambient pressure.

collapse, an improper dihedral-angle interaction potential has been proposed in [33, 34] as:

$$U_{\text{imp}} = \frac{K_\psi}{2}(\psi_k - \psi_0)^2, \tag{6}$$

where ψ is the improper dihedral angle that conserves the structure of chiral center in molecules modeled as united atoms. The corresponding forces cause the unit normal to the plane (C_1, C_2, C_3) to oscillate about its mean position. To match the equilibrium position obtained from MD simulations with explicit structure representation, an equilibrium value $\psi_0 = 35.04^\circ$ is used with the united atom potential. This is the angle formed with the –C_2–H– vector at equilibrium. Additionally, a value of equilibrium $\psi_0 = 0^\circ$ in the same functional form is used to maintain planarity of the phenyl ring.

The potential parameters for PS in table 1 are validated with density calculations at different temperatures, from which T_g for bulk PS is evaluated. For bulk PS, T_g is experimentally observed to be approximately 370 K [39]. For numerical evaluation, PS configurations at temperatures ranging from 480 to 200 K are simulated with a Berendsen NPT ensemble [40] (thermostatic constant $\tau_T = 1.0$ and barostatic constant $\tau_p = 5.0$) at a virial pressure of 1 atm. Figure 3 is a plot of specific volume, a property frequently used to calculate T_g, as a function of temperature. The slope of the curve in this figure signifies the coefficient of thermal expansion. This slope is observed to change in the vicinity of the experimentally observed value of 370 K. PS parameters are also validated with free-volume fraction f_v measurements that provide an alternative measure of T_g. The free-volume fraction is measured as the ratio of the accessible volume to the total volume, where the accessible volume is the difference between the measured unoccupied volume and the theoretical limit for the unoccupied volume in a system of randomly packed spheres.

The unoccupied volume is measured as the difference between the total simulation volume and the space filled by atoms, where each atom is manifested as a sphere with a radius equal to its van der Waals radius [41] given in table 1. The volume determining algorithm uses cubic voxels with a resolution of 0.01 Å. Figure 4 compares f_v from MD simulation with that from PALS data [29]. The change in slope of the curves, representing T_g, occurs at approximately the same temperature.

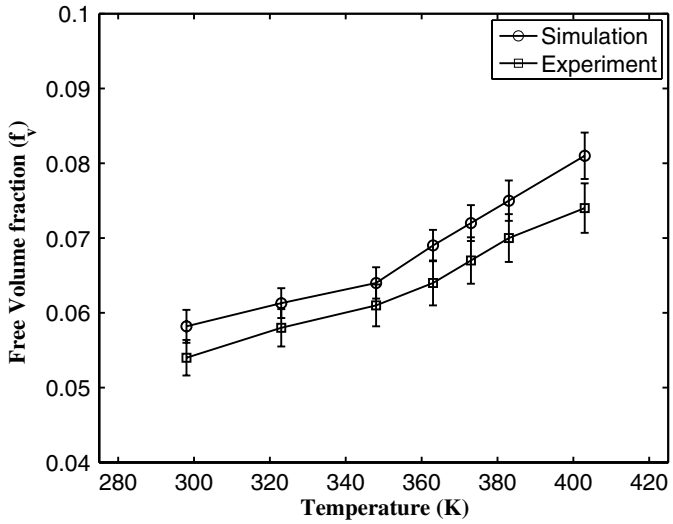

Figure 4. Variation of free-volume fraction distribution with temperature at ambient pressure. Error bars are shown in the figure.

Table 2. Potential function parameters for CO_2 molecule.

LJ Parameters	ε (kJ mol^{-1})	σ (Å)
C–C	0.5137	2.7570
O–O	0.8106	3.0330
C–O	0.6453	2.8920
Angular Bonds	k_θ (kJ mol^{-1} rad^{-2})	θ_0 (°)
O–C–O	1236	180.0
	Atom	q_i (e)
	C	+0.6512 (e)
	O	−0.3206 (e)

3.1.2. Representation of CO_2. Figure 2(*c*) shows a 3D structure of CO_2 molecule, modeled as a linear three atom molecule with two oxygen atoms sharing double bonds with a carbon atom in the middle. The elementary physical model (EPM2) potential [35] is used to model CO_2. This bonded potential molecule consists of rigid bonds and a flexible bond angle potential. The non-bonded and charged interaction are between atoms belonging to different CO_2 molecules. For the non-bonded van der Waals interactions, the LJ potential of equation (2) is used with parameters reported in table 2. Both the bond lengths (–O–C–) are kept fixed at 1.149 Å, and the angular potential for the –O–C–O– angle is explicitly modeled using a harmonic potential. The potential is given as

$$U_{nb}^{\mathrm{LJ}}(r_{ij}) = 4\varepsilon_{ij}\left[\left(\frac{\sigma_{ij}}{r_{ij}}\right)^{12} - \left(\frac{\sigma_{ij}}{r_{ij}}\right)^{6}\right] + \frac{K_\theta}{2}(\theta_k - \theta_0)^2 + \frac{q_i q_j}{4\pi\epsilon_0 r_{ij}}. \tag{7}$$

Values of ε_{ij}, σ_{ij}, K_θ and θ_0 and q (for carbon and oxygen) are listed in table 2.

Validation of the parameters for bulk CO_2 at supercritical conditions with EPM2 can be found in [42]. As an additional validation in this study, the diffusion coefficient is obtained from MD simulations using these parameters. The corresponding value is 2.17 $cm^2\ s^{-1}$, which is in good agreement with the value of 2.023 $cm^2\ s^{-1}$, obtained from the 17O NMR spin-lattice relaxation time measurements in [43].

3.1.3. PS–CO_2 interaction. The interaction between atoms of the PS molecules and atoms of CO_2 molecules govern important physical properties of the binary PS–CO_2 system being studied. Atoms involved in this interaction belong to different species of molecules without any covalent bond linking and hence, this interaction is non-bonded. It is important to implement validated functional forms for the interaction potentials for this binary system. Non-bonded interactions between pairs of atoms belonging to same molecule are conventionally modeled using the LJ potential [44] of equation (2). For non-bonded interactions between dissimilar atoms ($i \neq j$), the energy well depth (ϵ_{ij}) and the zero-potential distance parameter (σ_{ij}) should be determined according to an appropriate mixing rule. The Lorentz–Bertholet (LB) mixing-rule method [45], in which σ_{ij} is represented as the arithmetic mean and ϵ_{ij} as the geometric mean of the individual parameters respectively, is often used for modeling the LJ potential for dissimilar atoms.

The LB mixing rule based MD simulations however, do not yield satisfactory agreement with experimental results for f_v distribution at different temperatures and pressures. These simulations show an approximately 10% higher value of the bulk density in comparison with experiments. This discrepancy has also been noted in [46], where the LB mixing rule was found to underestimate σ_{ij} and overestimate ϵ_{ij} for pair interactions between atoms with significantly different parameters. This is expected to over-estimate the density values, especially at lower ranges of pressure and temperature. Similar observations have also been made in the trial simulations performed in this study. A different mixing rule is chosen to represent the PS–CO_2 inter-atomic non-bonded potential. This rule has been employed in [46] for inert gases and is based on the cubic mean for σ and the harmonic mean of the harmonic and geometric means for ϵ. This is denoted as the CM-HHG rule. The corresponding parameters are expressed as

$$\sigma_{ij} = \frac{\sigma_{ii}^3 + \sigma_{jj}^3}{\sigma_{ii}^2 + \sigma_{jj}^2}, \tag{8}$$

$$\epsilon_{ij} = \frac{2\sqrt{\epsilon_{ii}\epsilon_{jj}}\dfrac{2\epsilon_{ii}\epsilon_{jj}}{\epsilon_{ii}+\epsilon_{jj}}}{\sqrt{\epsilon_{ii}\epsilon_{jj}} + \dfrac{2\epsilon_{ii}\epsilon_{jj}}{\epsilon_{ii}+\epsilon_{jj}}} = \frac{4\epsilon_{ii}\epsilon_{jj}}{[\sqrt{\epsilon_{ii}}+\sqrt{\epsilon_{jj}}]^2}. \tag{9}$$

The choice of the CM-HHG mixing rule over the standard LB mixing rule has its roots in the statistical thermodynamics of polymer solution [47, 48]. In [47], the LB mixing rule is amended with empirical factors ξ and ζ for σ_{ij} and ϵ_{ij} respectively, for accurately calculating thermodynamical properties such as heat of mixing, critical solution temperature and chemical potential using lattice-fluid theory for polymer solutions. The factors ξ and ζ for the CM-HHG mixing rule are given as

$$\xi = \frac{\sigma_{ij}^{\text{CM-HHG}}}{\sigma_{ij}^{\text{LB}}} = 2\left[1 - \frac{\sigma_{ii}\sigma_{jj}}{\sigma_{ii}^2 + \sigma_{jj}^2}\right], \tag{10}$$

$$\zeta = \frac{\epsilon_{ij}^{\text{CM-HHG}}}{\epsilon_{ij}^{LB}} = \frac{4\sqrt{\epsilon_{ii}}\sqrt{\epsilon_{jj}}}{[\sqrt{\epsilon_{ii}}+\sqrt{\epsilon_{jj}}]^2}.$$

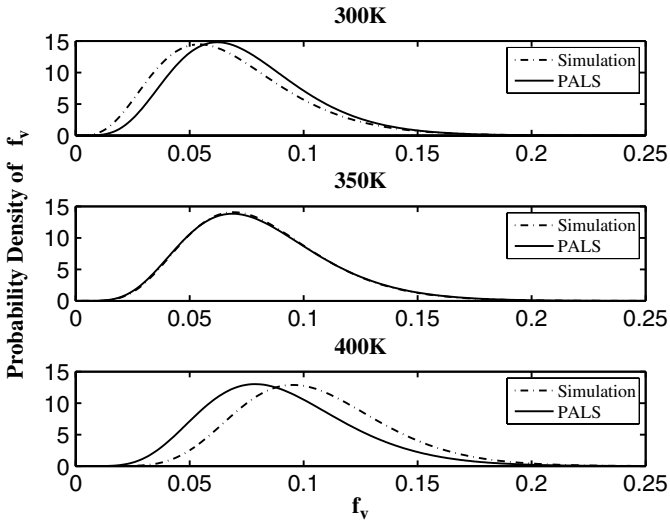

Figure 5. Comparison of f_v data from simulation with PALS results at ambient pressure.

Additionally, since $(\sigma_{ii}\sigma_{jj})/(\sigma_{ii}^2 + \sigma_{jj}^2) \leqslant \frac{1}{2}$ and $1 - \zeta = [\sqrt{\epsilon_{ii}} - \sqrt{\epsilon_{jj}}]^2/[\sqrt{\epsilon_{ii}} + \sqrt{\epsilon_{jj}}]^2 \geqslant 0.0$,

$$\xi \geqslant 1.0 \qquad \text{and} \qquad \zeta \leqslant 1.0. \tag{11}$$

Thus, the CM-HHG mixing rule gives a higher value of σ_{ij} and a lower value of ϵ_{ij} than that obtained by LB mixing rule, which are consistent with [47, 48].

To test the validity of the CM-HHG rule for PS–CO_2 interactions, a MD system with periodic boundary conditions is simulated with an NPT ensemble. The bulk density for the simulated binary system is within 5% of the experimentally observed value using the PALS setup. Figure 5 compares the distribution of f_v measurements at 300, 350 and 400 K. The experimental values are obtained by fitting data to a stochastic model assuming that the measurements sample a gamma distribution, expressed as

$$f(f_v) = \frac{\chi(\chi f_v)^{\beta-1}\exp^{(-\chi f_v)}}{\Gamma(\beta)}, \tag{12}$$

where $\Gamma(\beta)$ is the gamma function and β and χ are parameters whose values are determined by the following equations for the mean and mean-square fluctuations in f_v [28]:

$$\frac{\beta}{\chi} = E(f_v); \qquad \frac{\beta}{\chi^2} = E[(E(f_v) - f_v)^2]. \tag{13}$$

The simulation values are obtained by measuring the f_v at each snapshot over the simulation time, and fitting to the form given above. Excellent agreement is obtained near the glass transition temperature with this model. The errors at lower and higher temperatures are significantly less than those present for the model employing the LB mixing rule.

3.2. Steps in the MD simulation process

MD simulations are conducted with the software package DLPOLY, [49, 50] which employs an efficient domain decomposition parallelization strategy. Leapfrog Verlet time integration algorithms are used from the package [45] for integrating Newton's equations of motion.

3.2.1. Generation of initial system configurations. A number of polymer sample preparation methods, including rotational isomeric state (RIS) model [51–53] and Phantom chain growth (PCG) model [54, 55], are suggested in the literature to create and relax polymer chains with a bias toward the expected conformation. PCG method works well for polyethylene, where additional monomers are introduced based on a predetermined conditional probability with a random distribution of the dihedral angle for additional monomer. The change in energy ΔU, resulting from the introduction of a new site is determined by summing all the dihedral and non-bonded interactions. The acceptance criterion is expressed in terms of a probability p for this new site as

$$p = \min[1, [\exp(-\beta \Delta U)]], \tag{14}$$

where $\beta = 1/k_b T$, k_b is Boltzmann's constant and T the temperature of the system. If a new monomer segment is not acceptable, the chain is shortened by a single segment and the procedure is repeated again with another dihedral angle. A phenomenon that negatively affects the PCG algorithm during the creation of a large system in a fixed simulation box (8 PS chains with 320 monomers each in this model) is 'deadlocking'. In a deadlocked state, it becomes impossible to add new segments due to the absence of free space around the last segment. This occurs due to the high repulsive energy of the non-bonded interaction. The probability of deadlocking is high for PS, where large phenyl groups are attached to the backbone carbon atoms, and the presence of boundary atoms adds to this phenomenon.

In this work, an augmented PCG chain creation methodology is developed for PS to overcome this shortcoming by relaxing the acceptance criterion (14) in the energy increment at the site of occurrence. The increase in energy ΔU is recalculated without taking the affected phenyl side group into consideration. If the additional backbone atom is acceptable to the chain, the corresponding phenyl group is forced onto the chain at a later stage. This sometimes creates a high local energy which is taken care during chain relaxation process in the equilibration phase, as discussed in section 3.2.2.

The MD model incorporates PS systems with multiple chains. Eight PS chains with 320 monomers each are considered, which corresponds to 20488 united atoms. This 8×320 system size is chosen after conducting a size-effect analysis with respect to f_v. As seen in figure 6, the 8×320 system shows excellent agreement with PALS free-volume data as opposed to a smaller 8×80 system. The walls of the cubic simulation box of dimensions 120 Å $\times$ 120 Å $\times$ 120 Å, constitute of a layer of 9602 frozen atoms. During the chain creation, the repulsion from the boundary is turned on to keep the PS chain from exiting the boundary. Between atoms of different chains, the contribution to ΔU from the non-bonded potential is included to allow an initial separation between these atoms. After equilibrating the PS chains inside the simulation box, CO_2 molecules are introduced into the system.

A comprehensive assessment of different methodologies to apply pressure conditions on finite systems without applying a constant virial pressure is given in [23]. The reference for comparison is a finite system embedded in a classical fluid, which serves as a pressure reservoir. The fluid is prevented from diffusing into the finite system by intermolecular repulsion. In this work, an additional challenge comes from the fact that the pressure-inducing agent (CO_2) is also a solvent. Consequently, a novel PS–CO_2 simulation model is designed with CO_2 as both a plasticizing and a pressure-inducing agent.

The number of CO_2 molecules in the simulation box is initially estimated using the van der Waals equation of state for real gases, i.e.

$$\left(p + \frac{n^2 a}{V^2}\right)(V - nb) = nRT, \tag{15}$$

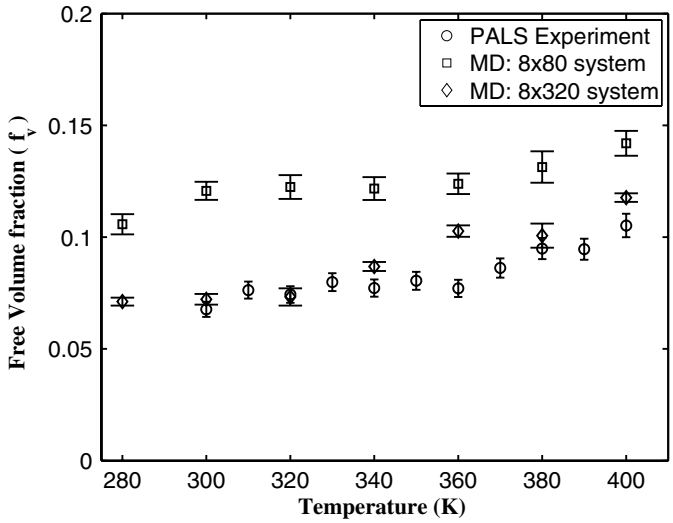

Figure 6. Free-volume fraction, with error bars, at 400 psi as a function of temperature for different system sizes.

where p is the pressure, V is the volume of the simulation box, n is the number of CO_2 molecules, R is the gas constant (8.314 J K^{-1} mole^{-1}), T is the temperature and a and b are empirical parameters for the real gas. Equation (15) accounts for non-bonded interactions between atoms in real gases. The values of the constants a and b for CO_2 used here are 0.3643 J m^3 mole^{-1} and 4.25×10^{-5} m^3 mole^{-1}, respectively. Independent MD simulations are subsequently carried out to attain a virial CO_2 pressure inside the simulation box, expressed as

$$p = \frac{1}{V}\left(nRT + \frac{1}{3}\sum_{i,j(i\leqslant j)}\overline{F_{ij}\cdot r_{ij}}\right). \tag{16}$$

The second term on the right-hand side includes the time averaged (marked by the overline) work done by the force F_{ij} exerted by atom i on atom j due to the displacement by their relative distance r_{ij}. The first part of this equation is the ideal gas contribution. Figure 7 shows the results of the pressure calibration, where the value calculated by the van der Waals equation (15) is observed to deviate from the simulation values. Using the form of the van der Waals equation, but with parameter values suggested by the simulation results, the number of CO_2 molecules necessary to achieve a desired system pressure is calculated.

Once the number of molecules required to maintain a given pressure at 300 K is determined, the simulation box is populated. The number of molecules in the box is kept fixed throughout the simulation process. The simulation time is too short to allow for much diffusion of CO_2 into or out of the PS sample. Consequently, the volume fraction of CO_2 is maintained independently of temperature. It is assumed that the deviations in the instantaneous pressures from the initial values do not have a significant effect on the amount of CO_2 absorbed in the PS ensemble. Indeed, examination of the CO_2 density profile within PS shows little fluctuation across the range of temperatures simulated. A typical PS–CO_2 molecular system at 400 K with an initial pressure of 400 psi is shown in figure 8. This system has 1528 CO_2 molecules. Table 3 lists the systems considered with different number of CO_2 molecules for different pressures and volumes.

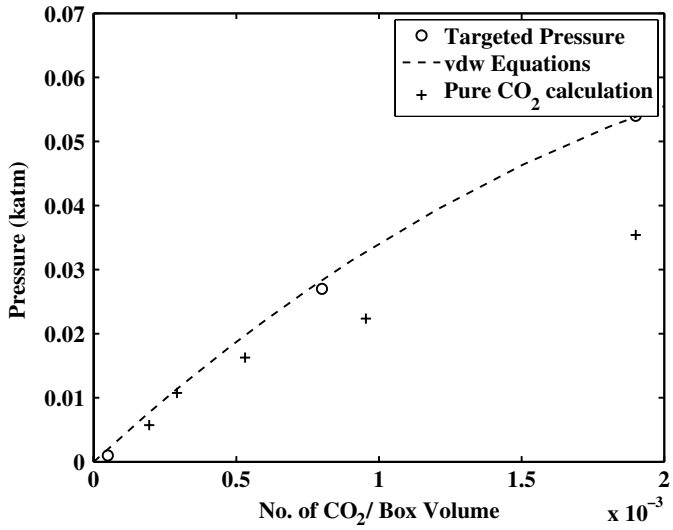

Figure 7. Calibration of pressure at 300 K due to CO_2 in the walled structure.

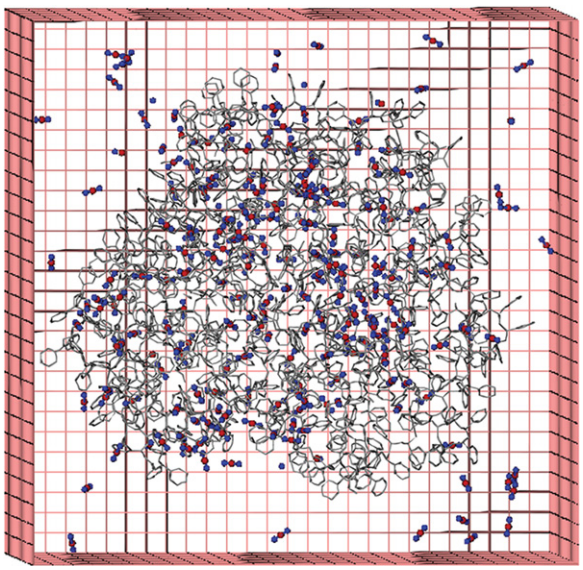

Figure 8. A schematic of MD setup for finite PS–CO_2 system where the boundary is represented with repulsive walls.

Table 3. Number of CO_2 at 300 K for different pressures for two simulation volumes.

Pressure (psi)	0.0	14.7	400.0	800.0
8 × 80 PS	0	14	380	950
8 × 320 PS	0	50	1528	3676

3.2.2. Dynamic system relaxation with equilibration. Prior to the MD simulations, dynamic relaxation of the binary PS–CO_2 system is conducted to arrive at an equilibrated initial configuration. The system is allowed to relax at 600 K for approximately 5–10 ns, depending on chain length, until the final equilibrated structure is produced. The steeply rising repulsive wall at distances $r_{ij} \leqslant \sigma_{ij}$ often gives rise to numerical instabilities and a gradual introduction of the excluded volume effects have been proposed in the relaxation method. Non-bonded forces from the pair potentials are slowly increased in these methods by slowly incrementing σ_{ij} from a small value to its actual value. Despite reducing σ_{ij}, the problem of huge repulsive forces can persist if atom pair distances approach zero due to the inverse relation with high exponent. This situation especially manifests for periodic bulk systems, in which atoms belonging to polymer chains can overlap with those in the boundary images generated to simulate periodicity conditions. A regularization based force-capping method, proposed in [56] and discussed in [41], is used in this work to circumvent this limitation. In this method, the non-bonded LJ potential is modified to introduce force capping, given as

$$U_{nb}^{\text{fc-LJ}}(r) = \begin{cases} U_{nb}^{\text{LJ}}(r_c) + \frac{\mathrm{d}U_{nb}^{\text{LJ}}(r)}{\mathrm{d}r}\,|_{r_c}\,(r - r_c)\forall r, & 0 \leqslant r \leqslant r_c, \\ U_{nb}^{\text{LJ}}(r)\ \forall r, & r > r_c. \end{cases} \tag{17}$$

The capping distance r_c is set to a value that yields a prescribed value of the non-bonded force at this distance, i.e. $-\frac{\mathrm{d}U_{nb}^{\text{LJ}}(r)}{\mathrm{d}r}|_{r_c} = f_c$. Correspondingly, $r_c \longrightarrow 0$ for $f_c \gg 1$ and $r_c \longrightarrow 0$ for $f_c \longrightarrow 0$. For $r < r_c$, equation (17) implies a much weaker linear increase resulting in a finite penalty energy for $r = 0$. In the equilibration process, r_c is gradually reduced from the LJ cutoff radius $r_c = 2^{\frac{1}{6}}\sigma$ to 0.8σ which is significantly smaller than relevant inter-atomic distances. An important consideration in MD simulation of large polymers is the wide range of relaxation time scale at which they operate. While local segmental motions like orientation of side groups or end group movements may exhibit a time scale of less than 10 ps, overall chain dimensions may have much longer relaxation time, as much as 0.2 μs.

3.2.3. System simulation. The finite system MD model, as shown in figure 8, is simulated with the Evans NVT ensemble. PS is modeled in a vacuum (0 psi) and in three different CO_2 pressure conditions, namely, 14.7, 400 and 800 psi. In order to represent the range of PS behavior from liquid to amorphous solid, simulations are performed in the decreasing temperature range 480–200 K, at intervals of 20 K, for each of the four pressure conditions. Each step in the cooling process is simulated for 1 ns with a time step of 1 fs. This cooling rate is consistent with previous studies by the authors in [41]. Figure 9 shows the convergence of density in the MD simulation. The simulation and experimental cooling rates differ by many orders of magnitude. However, MD simulations are typically limited by the duration. An assumption made in this study is that in the limit of extremely slow cooling rates, the densities and in turn the T_g stay true to the one exhibited by the simulated cooling rate. It is shown [41] that the density stabilizes within the simulation time range, and a longer duration would imply more computational cost without any significant change in density. Consequently, the system is equilibrated at each temperature for 1 ns, when the specific volume is found to converge to a stable value.

4. Results and discussion

The MD model is used to study the effect of CO_2 on the glass transition temperature T_g of PS at a range of pressures. This study is intended to identify and understand the underlying physical mechanisms that facilitate the reduction in T_g. The MD simulation data are processed

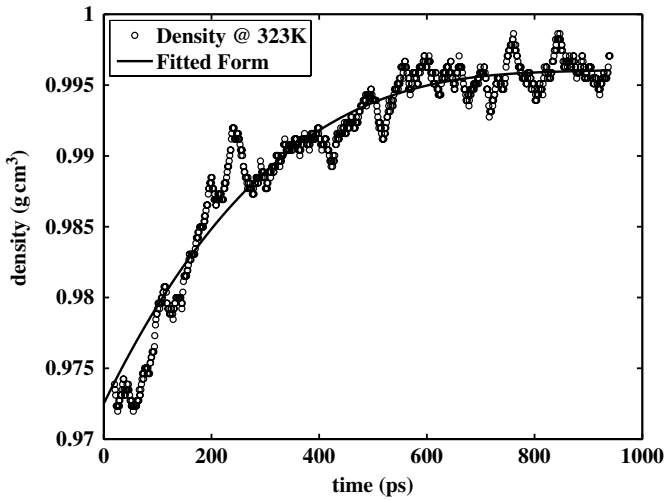

Figure 9. Evolution of density as the PS system is cooled from 348 to 323 K for a duration of 1 ns (cooling rate of 0.05 K ps^{-1}). The density converges after around 1 ns and further cooling does not cause any additional change in density.

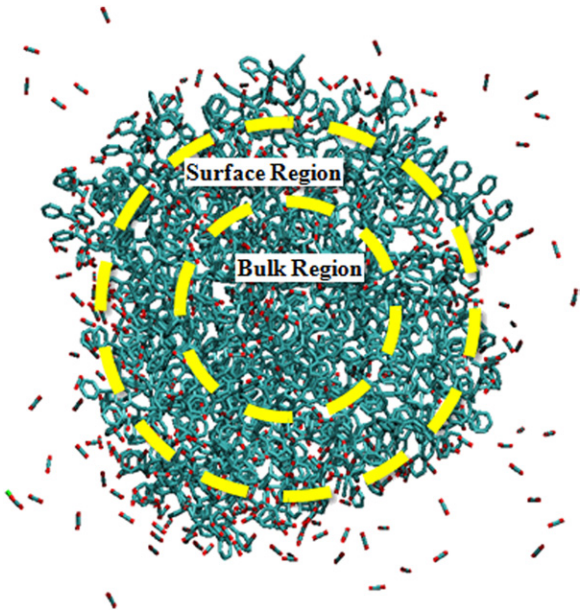

Figure 10. Schematic of surface and bulk zones (based on density and free-volume fraction variations).

to analyze physical properties such as free-volume fraction f_v, density ρ and mobility at each temperature. For determining gradients in f_v and ρ through the cross-section, the simulation volume in figure 10 is divided into a series of spherical shells. This process helps delineate surface and bulk regions, necessary to establish bulk and surface properties.

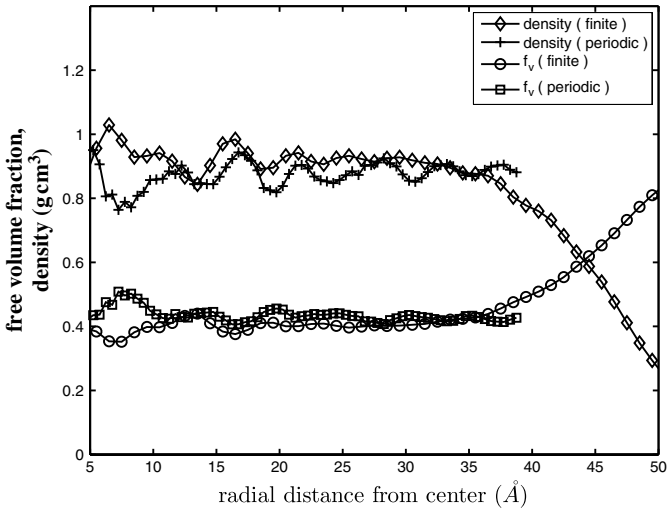

Figure 11. Variation of density and free-volume fraction as a distance from center for finite system at 400 K and 400 psi of CO_2 pressure and comparison with bulk results from PBC system with same configurations.

4.1. Effect of CO_2 on T_g of bulk PS

Results of the PALS experiments in figure 1(*b*) demonstrate that T_g of bulk PS system decreases with increasing CO_2 pressure. The simulation based T_g of the bulk PS–CO_2 system is evaluated from analysis at the central core, as shown in figure 10. The extent of the core region is easily identifiable from the gradients in ρ and f_v, as shown in figure 11. At low radial distances, the density plot shows fluctuations that are indicative of lack of a statistically sufficient number of molecules in this region to form a representative volume. The density stabilizes to a value similar to those observed in periodic bulk systems in the range 10–30 Å. Beyond 30 Å, the density rapidly decreases, indicating surface effects of the molecular system. Similar trends are also seen in the free-volume fraction behavior in figure 11. A spherical core region with a 20 Å radius corresponds to the largest volume for which the studied properties are stable for all temperature and CO_2 pressure conditions. Consequently, this region may be used consistently for the evaluation of the bulk behavior of the binary systems. It is evident from figure 12 that for higher CO_2 pressures, the specific volume measured in the core is higher. This implies swelling in the experimentally measured system. Additionally, the data in figure 13 show that increasing CO_2 pressure alters the shape of the density profile at the surface.

The glass transition temperature of PS in the presence of CO_2 is evaluated from the specific volume (ρ^{-1}) calculations at different temperatures and CO_2 pressure conditions. These values are further corroborated by f_v calculations. Figure 12 shows the variation of ρ^{-1} at CO_2 pressures of 14.7, 400 and 800 psi. Two important observations are made from these plots. First, for a given temperature, the specific volume is found to increase significantly with CO_2 pressure. Second, the temperature at which the slope of the specific volume curve shows a sharp change decreases with increasing CO_2 pressure. The slope is identified with the thermal expansion coefficient of PS. Higher specific volume with increasing CO_2 pressure creates a larger free volume. This indicates that CO_2 plasticizes the PS, causing increased mobility at higher pressures, resulting in a switch from amorphous solid to liquid state even at a lower temperature. The knee in figure 12 is representative of T_g, corresponding to a

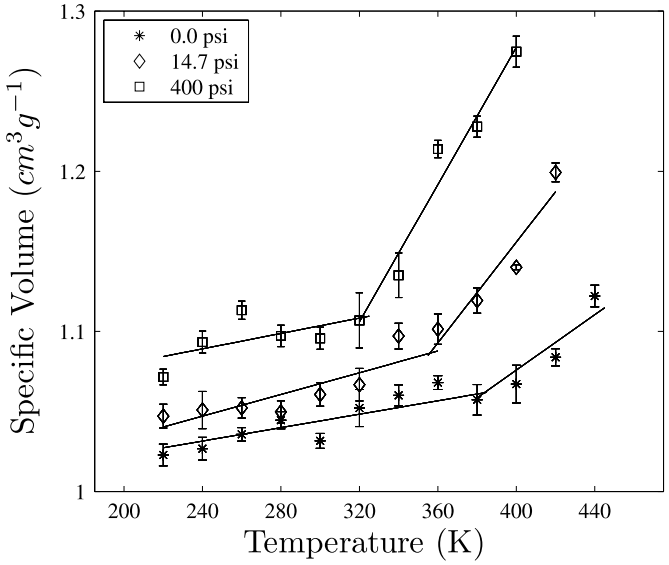

Figure 12. Glass transition point identification by plotting specific volume against temperature for finite systems with different CO_2 pressures. Standard deviation in measurements is shown by error bars.

rapid change in the dependence of specific volume on temperature. Figure 14 compares the MD simulated T_g results of this model with that from the Wissinger–Paulaitis model [12] as well as PALS experiments, as a function of CO_2 pressure [11]. Good agreement between the models and the experimental data is observed, with a maximum difference of ∼10% for all pressure conditions. A possible source of this small discrepancy is the difference in resolutions between the experiments and simulation. The smallest detectable void inherent to the PALS method (∼1.6 Å) in contrast with the simulation resolution of 0.01 Å. The difference with the Wissinger–Paulaitis model is attributed to the different methods of T_g measurements. T_g in the Wissinger–Paulaitis model is determined from creep compliance measurement as a function of time at constant pressure and temperature.

4.2. Transition characteristics from bulk to surface response

The surface layer in this study is identified from the onset of deviation in ρ and f_v from the bulk behavior, as demonstrated in figure 11. The variation of simulated ρ with radial distance is plotted for three CO_2 pressure conditions in figure 13. The surface region is assumed to begin from the location at which ρ decreases to 90% of the value in the stable core region. This region continues until ρ is less than 5% of the core value. Figure 15 shows the extent of the surface region for two pressure conditions and two temperatures. It is shown that the extent of the surface layer increases both with rising temperature and higher amounts of CO_2. However, the enthalpic gain due to the addition of CO_2 outweighs the entropic gain due to increased temperature. Furthermore, the impact of the CO_2 on the density of the polymer is more localized to the surface than the effect due to increased temperature. Quantification of the extent of the surface layer in the presence of CO_2 can be used to determine conditions that preferentially influence the surface properties with little disturbance to the core region. This effect is very important for processing devices with precise nanoscale geometries, allowing

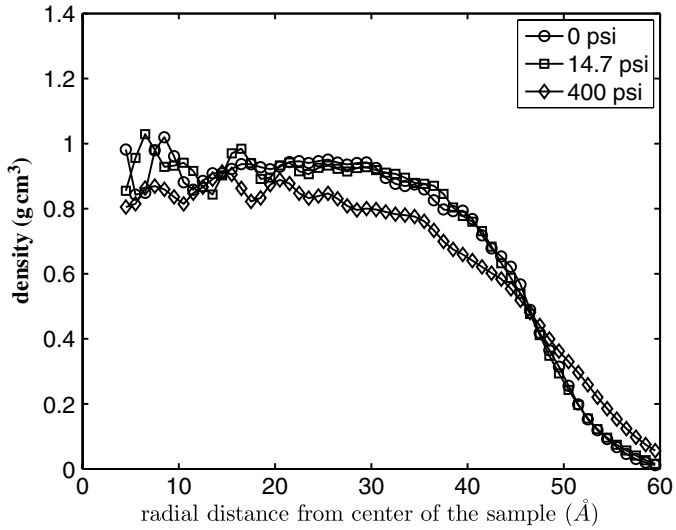

Figure 13. Density variation across thickness at 400 K and different pressures of CO_2.

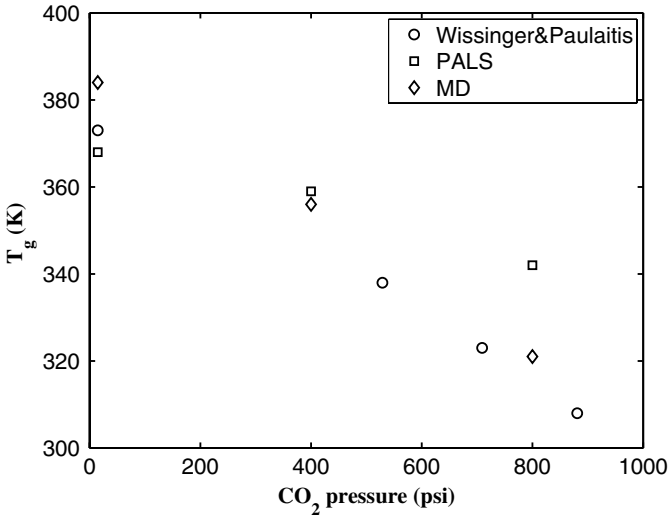

Figure 14. Glass transition temperature variation with CO_2 at different pressures of CO_2. Error in the data presented here is bounded by the error shown in figure 12.

greater control over the formation and bonding processes, which in turn allows the reduction in size of these devices to critical scales.

Mobility analysis is conducted by calculating the root-mean-square (RMS) displacement of the PS atoms belonging to different layers along the radial distance. This can be used to identify the surface layer. The random motion of atoms and molecules within a given volume is represented adequately by the RMS displacement. This is expressed as a measure of the

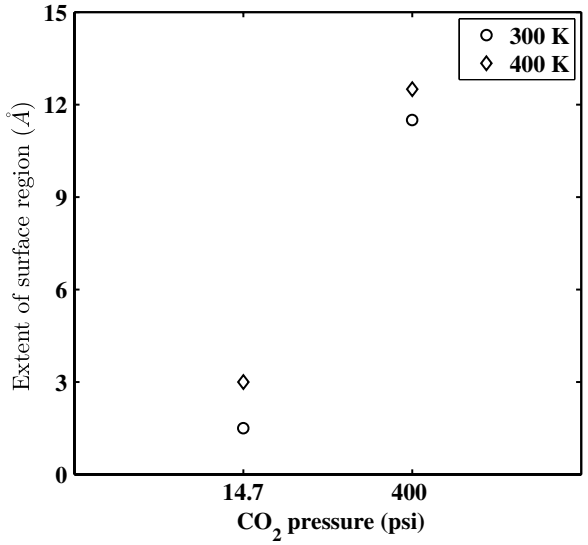

Figure 15. Depth of free surface region as measured from the PS outer surface as a function of CO_2 pressure for two temperatures. The error (not shown) is <3% for all data points.

distance an atom or molecule travels in a given time,

$$\mathrm{RMS}(t) = \sqrt{\frac{\sum_{i=1}^{N}[(x_i(t) - x_i(0))^2 + (y_i(t) - y_i(0))^2 + (z_i(t) - z_i(0))^2]}{N}}, \tag{18}$$

where N is the number of atoms and $(x_i(t), y_i(t), z_i(t))$ are time dependent coordinates of the ith atom. Figure 16 shows the RMS displacements for PS atoms along the radial distance for a duration of 25 ps at CO_2 pressure of 400 psi for three temperatures. For temperatures of 260, 340 and 420 K, a gradient in RMS displacement appears along the radial direction. This signifies that the surface PS atoms are more mobile than those in the core region. This trend is in accordance with the density gradient in figure 11, which also seems to drop from $r \geqslant 30$ Å. This observation agrees well with the theory that PS surface regions in PS have higher mobility and lower density.

Another interesting observation is made with respect to the position of the PS chain ends. Figure 17 plots the average position of the 16 chain ends at CO_2 pressure of 400 psi. While the initial positions of chain ends are randomly spread across the system, the figure shows that chain ends tend to migrate toward the surface with time. This effect is more pronounced at temperatures higher than T_g. In accordance with earlier studies [57, 58], it is observed that this surface enrichment of chain end groups facilitates the increase in free volume at the surface as shown in figure 11.

5. Conclusions

An experimentally validated MD model is developed in this study to predict the T_g of a nanoscale sample of PS in the presence of CO_2. The computational system is calibrated for pressure control through monitoring of the number of CO_2 molecules within the finite simulation volume. Surface and bulk regions are identified via gradients in density and fractional free volume, and the behaviors of each are captured simultaneously and analyzed

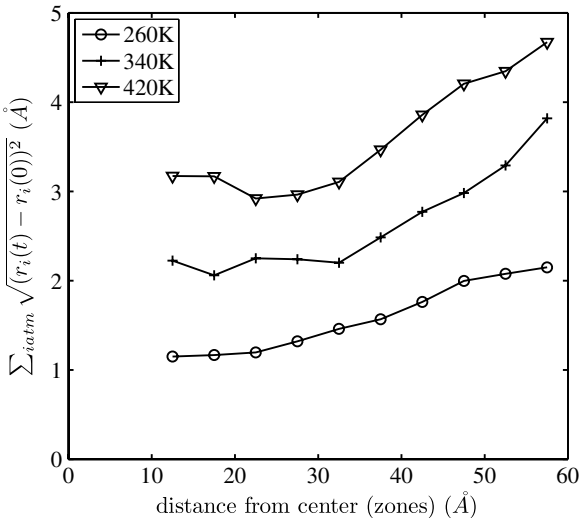

Figure 16. RMS displacement in different layers of PS–CO_2 systems at 400 psi for a duration of 25 ps.

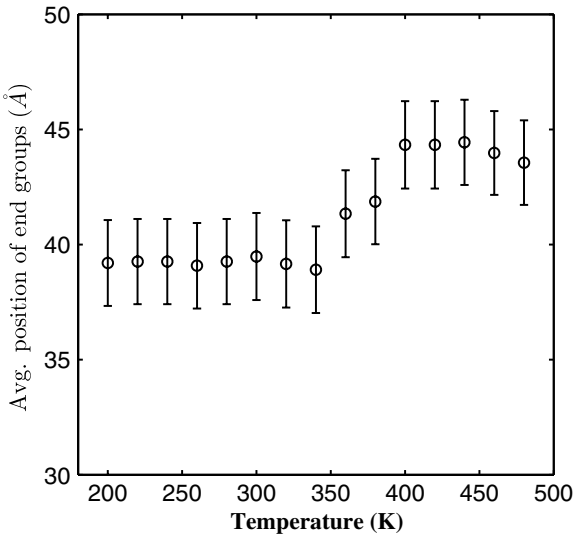

Figure 17. Variation in mean position of end groups of the PS chain with rising temperature at 400 psi CO_2 pressure. Error bars are shown in the figure.

within a single model. Data extracted from the bulk core region are compared with the PALS-based experimental data for free-volume fraction [11]. The model is able to accurately predict changes in T_g with changing CO_2 pressure. Observations made in the surface region indicate surface enrichment of end groups, which can be used as an indicator of optimal bonding conditions, corresponding to a preferentially softened surface layer. Additionally, a marked increase in segmental chain mobility at the surface causes it to behave in a more fluid-like manner compared with the core even below T_g. This mobility characteristic enables geometry-preserving bonding techniques for nanoscale devices using high pressure CO_2. The model

developed in this study can be extended to polymeric thin films, which is the subject of a forthcoming paper.

Acknowledgments

This work has been supported by the NSF Division of Engineering Education and Centers through grant no EEC-0425626 to the Center for Affordable Nanoengineering of Polymeric Biomedical Devices (CANPBD) at the Ohio State University (Professor James Lee, Director). This sponsorship is gratefully acknowledged. Computer support by the Ohio Supercomputer Center through grant PAS813-2 is also gratefully acknowledged.

References

[1] Chou S, Krauss P R and Renstrom P J 1995 *Appl. Phys. Lett.* **67** 3114
[2] Seliger R, Ward J W, Wang V and Kubena R L 1979 *Appl. Phys. Lett.* **34** 310
[3] Piner R D, Zhu J, Xu F, Hong S and Mirkin C A 1999 *Science* **283** 661
[4] Abramowitz H, Shah P S, Green P F and Johnston K P 2004 *Macromolecules* **37** 7316
[5] Pai R, Humayun R, Schulberg M T, Sengupta A, Sun J and Watkins J J 2004 *Science* **303** 507
[6] Yang Y, Lui D, Xie Y, Lee L J and Tomasko D L 2007 *Adv. Mater.* **19** 251
[7] Cooper A I 2000 *J. Mater. Chem.* **10** 207
[8] Nalwade S, Picchioni F and Janssen L 2006 *Prog. Polym. Sci.* **31** 19
[9] Kazarian S G, Vincent M F, Liotta C L and Eckert C A 1996 *J. Am. Chem. Soc.* **118** 1729–36
[10] Yang Y 2005 Polmer carbon dioxide *PhD Thesis* The Ohio State University
[11] Chen H M, Cheng M L, Jean Y C, Lee J L and Yang J T 2008 *J. Polym. Sci.* B **46** 388
[12] Wissinger R G and Paulaitis M E 1991 *J. Polym. Sci.* B **29** 631
[13] Wissinger R G and Paulaitis M E 1991 *Ind. Eng. Chem. Res.* **30** 842
[14] Condo P D, Sanchez I C, Panayiotou C G and Johnston K P 1992 *Macromolecules* **25** 6119
[15] Condo P D, Paul D R and Johnston K P 1994 *Macromolecules* **27** 365
[16] Kwag C, Manke C W and Gulari E 2001 *Ind. Eng. Chem. Res.* **40** 3048
[17] Rigby D and Roe R J 1990 *Macromolecules* **23** 5312
[18] Binder K, Müller M, Virnau P and MacDowell L G 2005 *Adv. Polym. Sci.* **173** 1–105
[19] Jain T and de Pablo J 2002 *Macromolecules* **35** 2167
[20] Morita H, Tanaka K, Kajiyama T, Nishi T and Doi M 2006 *Macromolecules* **39** 6233–7
[21] Lyulin A V and Michels M A J 2002 *Macromolecules* **35** 1463
[22] Martonak R, Molteni C and Parinello M 2000 *Phys. Rev. Lett.* **84** 682
[23] Baltazar S E, Romero A H, Rodriguez-Lopez J L, Terrones H and Martonak R 2006 *Comput. Mater. Sci.* **37** 526
[24] Takeuchi H and Okazaki K 1990 *J. Chem. Phys.* **92** 5643
[25] Han J and Boyd R H 1996 *Polymer* **37** 1797
[26] Pavel D and Shanks R 2003 *Polymer* **44** 6713
[27] Eslami H and Plathe F M 2007 *Macromolecules* **40** 6413
[28] Jean Y C 1990 *Microchemical J.* **42** 72
[29] Jean Y C, Sandreczki T C and Ames D P 1986 *J. Polym. Sci.* B **24** 1247
[30] Nakaniehi H, Wang S and Jean Y C 1988 *World Sci.: Singapore* **292** 292
[31] Hong X, Jean Y C, Yang S, Jordon S S and Koros W J 1996 *Macromolecules* **29** 7859
[32] Yuan J, Cao H, Hellmuth E W and Jean Y C 1998 *J. Polym. Sci.* B **36** 3049
[33] Harmandaris V A, Adhikari N P, van der Vegt N F A and Kremer K 2006 *Macromolecules* **39** 6708
[34] Wick C D, Martin M G and Siepmann J I 2000 *J. Phys. Chem.* B **104** 8008
[35] Harris J G and Yung K H 1995 *J. Phys. Chem.* **99** 12021
[36] Toxvaerd S 1990 *J. Chem. Phys.* **93** 4290
[37] Han J, Gee R H and Boyd R H 1994 *Macromolecules* **27** 7781
[38] Ryckaert J P, Ciccotti G and Berendsen H J C 1977 *J. Comput. Phys.* **23** 327
[39] Osswald T A and Menges G 2003 *Materials Science of Polymers for Engineers* (New York: Hansen & Gardner)
[40] Berendsen H J C, Postma J P M, van Gunsteren W, DiNola A and Haak J R 1984 *J. Chem. Phys.* **81** 3684
[41] Srivastava A and Ghosh S 2009 *Int. J. Multiscale Comput. Eng.* at press
[42] Saharay M and Balasubramanian S 2004 *J. Chem. Phys.* **120** 9694–702
[43] Etesse P, Zega J A and Kobayashi R 1992 *J. Chem. Phys.* **97** 2022

[44] Lennard-Jones J E 1924 *Proc. R. Soc* **106** 463
[45] Allen M P and Tindsley D J 2002 *Computer Simulation of Liquids* (Oxford: Oxford Science Publications)
[46] Halgren T A 1992 *J. Am. Chem. Soc.* **114** 7827
[47] Sanchez I C and Lacombe R H 1978 *Macromolecules* **11** 1145
[48] Zhong C and Masuoka H 1998 *Fluid Phase Equilibra* **144** 49
[49] Smith W and Forester T J 1996 *Molecular Graphics* **14** 136
[50] Todorov I and Smith W 2004 *Phil. Trans. R. Soc. Lond.* A **362** 115
[51] Flory P 1969 *Statistical Mechanics of Chain Molecules* (New York: Wiley Interscience)
[52] Rapold R F and Suter U W 1994 *Macromolecule Theory and Simulation* **3** 1
[53] Rapold R F, Suter U W and Theodorou D N 1994 *Macromolecule Theory and Simulation* **3** 19
[54] McKechnie J I, Brown D and Clarke J H R 1992 *Macromolecules* **25** 1562
[55] Brown D, Clarke H R, Okuda M and Yamazaki T 1994 *J. Chem. Phys.* **8** 6011
[56] Auhl R, Everaers R, Grest G S, Kremer K and Plimpton S J 2003 *J. Chem. Phys.* **119** 12718
[57] de Gennes P G 1988 *C. R. Acad. Sci. (Paris) II* **307** 1841–44
[58] Jiang X, Yang C Z, Tanaka K, Takahara A and Kajiyama T 2001 *Phys. Lett.* A **281** 363–7